
The Frontier of Reionization: Theory and Forthcoming Observations

Abraham Loeb

Harvard University, CfA, MS 51, 60 Garden Street, Cambridge MA 02138,
aloeb@cfa.harvard.edu

Summary. The cosmic microwave background provides an image of the Universe 0.4 million years after the Big Bang, when atomic hydrogen formed out of free electrons and protons. One of the primary goals of observational cosmology is to obtain follow-up images of the Universe during the epoch of reionization, hundreds of millions of years later, when cosmic hydrogen was ionized once again by the UV photons emitted from the first galaxies. To achieve this goal, new observatories are being constructed, including low-frequency radio arrays capable of mapping cosmic hydrogen through its redshifted 21cm emission, as well as imagers of the first galaxies such as the *James Webb Space Telescope (JWST)* and large aperture ground-based telescopes. The construction of these observatories is being motivated by a rapidly growing body of theoretical work. Numerical simulations of reionization are starting to achieve the dynamical range required to resolve galactic sources across the scale of hundreds of comoving Mpc, larger than the biggest ionized regions.

1 Preface

When we look at our image reflected off a mirror at a distance of 1 meter, we see the way we looked 6.7 nanoseconds ago, the light travel time to the mirror and back. If the mirror is spaced 10^{19} cm \simeq 3 pc away, we will see the way we looked twenty-one years ago. Light propagates at a finite speed, and so by observing distant regions, we are able to see what the Universe looked like in the past, a light travel time ago. The statistical homogeneity of the Universe on large scales guarantees that what we see far away is a fair statistical representation of the conditions that were present in our region of the Universe a long time ago. This fortunate situation makes cosmology an empirical science. We do not need to guess how the Universe evolved. Using telescopes we can simply see how the Universe appeared at earlier cosmic times. In principle, this allows the entire 13.7 billion year cosmic history of our Universe to be reconstructed by surveying galaxies and other sources of light out to large distances. From these great distances, the wavelength of the emitted radiation is stretched by a large redshift factor $(1+z)$ until it is observed, owing to the expansion of the Universe. Since a greater distance means a fainter flux from a source of a fixed luminosity, the observation of the earliest, highest-redshift sources of light requires the development of sensitive infrared telescopes such as the *James Webb Space Telescope (JWST)*.

Our cosmic photo album contains an early image of the Universe when it was 0.4 million years old in the form of the cosmic microwave background (CMB) [10, 100], as well as many

snapshots of galaxies more than a billion years later ($z < 6$; see overview in Ref. [33]). But we are still missing some crucial pages in this album. In between these two epochs was a period when the Universe was dark, stars had not yet formed, and the cosmic microwave background no longer traced the distribution of matter. And this is precisely the most interesting period, when the primordial soup evolved into the rich zoo of objects we now see. The situation that cosmologists face is similar to having a photo album of a person that contains the first ultrasound image of him or her as an unborn baby and some additional photos as a teenager and an adult. If you tried to guess from these pictures what happened in the interim, you could be seriously wrong. A child is not simply a scaled-up fetus or scaled-down adult. The same is true with galaxies. They did not follow a straightforward path of development from the incipient matter clumping evident in the microwave background.

2 Preliminaries

About 400,000 years after the Big Bang the temperature of the Universe dipped for the first time below a few thousand degrees Kelvin. The protons and electrons were then sufficiently cold to recombine into hydrogen atoms. It was just before the moment of cosmic recombination (when matter started to dominate in energy density over radiation) that gravity started to amplify the tiny fluctuations in temperature and density observed in the CMB data [100]. Regions that started out slightly denser than average began to contract because the gravitational forces were also slightly stronger than average in these regions. Eventually, after hundreds of millions of years of contraction, galaxies and the stars within them were able to form.

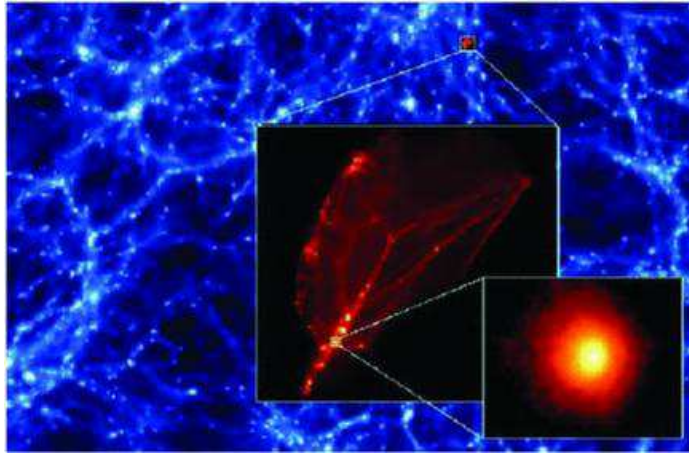


Fig. 1. A slice through a numerical simulation of the first dark matter condensations to form in the Universe (from Diemand, Moore, & Stadel 2005). Colors represent the dark matter density at $z = 26$. The simulated volume is 60 comoving pc on a side, simulated with 64 million particles each weighing $1.2 \times 10^{-10} M_{\odot}$.

The detailed statistical properties of the CMB anisotropies [100] indicate that indeed the structure apparent in the present-day Universe was seeded by small-amplitude inhom-

geneities, mostly likely induced by quantum fluctuations during the early epoch of inflation. The growth of structure from these seeds was enhanced by the presence of dark matter – an unknown substance that makes up the vast majority (84%) of the cosmic density of matter. The motion of stars and gas around the centers of nearby galaxies indicates that each is surrounded by an extended mass of dark matter, and so dynamically-relaxed dark matter concentrations are generally referred to as “halos”.

Under the assumption that general relativity describes the evolution of the Universe, the measured CMB anisotropies indicate conclusively that most of the matter in the Universe must be very weakly coupled to electromagnetism and hence cannot be the matter that we are made of (baryons). This follows from the fact that prior to hydrogen recombination, the cosmic plasma was coupled to the radiation through Thomson scattering. Small-scale fluctuations were then damped in the radiation-baryon fluid by photon diffusion. The damping is apparent in the observed suppression of the CMB anisotropies on angular scales well below a degree on the sky, corresponding to spatial scales much smaller than 200 comoving Mpc. To put this scale in context, the matter that makes up galaxies was assembled from scales of < 2 Mpc. In order to preserve the primordial inhomogeneities that seeded the formation of galaxies, it is necessary to have a dominant matter component that does not couple to the radiation fluid. The most popular candidate for making up this component is a weakly interacting massive particle (WIMP). If this particle is the lightest supersymmetric particle, it might be discovered over the coming decade in the data stream from the *Large Hadron Collider*.

The natural temperature for the decoupling of WIMPs is expected to be high (tens of MeV), allowing them to cool to an extremely low temperature by the present epoch. The resulting *Cold Dark Matter (CDM)* is expected to fragment down to a Jupiter mass scale [30, 69, 11]. The baryons, however, cannot follow the CDM on small scales because of their higher thermal pressure. The minimum scale for the fragmentation of the baryons, the so-called “filtering scale” (which is a time-averaged Jeans mass), corresponds to $\sim 10^5 M_\odot$ prior to reionization [65].

2.1 The First Stars

For the scale-invariant Λ CDM power spectrum [100], the first dark matter halos to contain gas have formed at a redshift of several tens. The assembly and cooling of gas in these halos resulted in the formation of the first stars [19]. Hydrodynamical simulations indicate that the primordial (metal-free) gas cooled via the radiative transitions of molecules such as H_2 and HD down to a temperature floor of a few hundred K, dictated by the energy levels of these molecules. At the characteristic density interior to the host clouds, the gas fragmented generically into massive ($> 100 M_\odot$) clumps which served as the progenitors of the first stars. The relatively high sound speed (c_s) resulted in a high accretion rate ($\dot{M} \sim c_s^3/G$ over the stellar lifetime of a few million years) and a high characteristic mass for the first (so-called *Population III*) stars [22, 1]. The lowest-mass halos most likely hosted one star per halo.

Population III stars in the mass range of 140–260 M_\odot led to pair-instability supernovae that enriched the surrounding gas with heavy elements [51]. Enrichment of the gas to a carbon or oxygen abundance beyond $\sim 10^{-3.5} Z_\odot$ resulted in efficient cooling and fragmentation of the gas to lower-mass stars [20, 40, 88]. The hierarchical growth in halo mass eventually led to the formation of halos with a virial temperature of $\sim 10^4$ K in which cooling was mediated by atomic transitions. Fragmentation of gas in these halos could have led to the direct formation of the seeds for quasar black holes [21, 66].

A massive metal-free star is an efficient factory for the production of ionizing photons. Its surface temperature ($\sim 10^5$ K) and emission spectrum per unit mass are nearly independent of

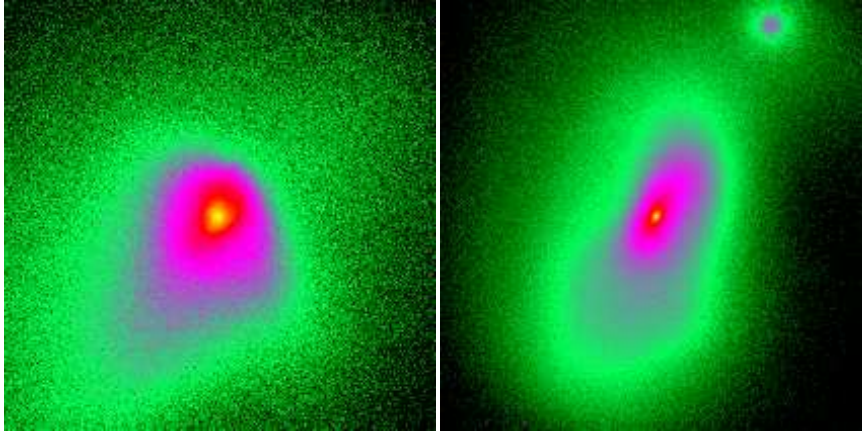


Fig. 2. Collapse and fragmentation of a primordial cloud (from Bromm & Loeb 2004). Shown is the projected gas density at a redshift $z \simeq 21.5$, briefly after gravitational runaway collapse has commenced in the center of the cloud. *Left:* The coarse-grained morphology in a box with linear physical size of 23.5 pc. At this time in the unrefined simulation, a high-density clump (sink particle) has formed with an initial mass of $\sim 10^3 M_\odot$. *Right:* The refined morphology in a box with linear physical size of 0.5 pc. The central density peak, vigorously gaining mass by accretion, is accompanied by a secondary clump.

its mass above a few hundred M_\odot , as it radiates at the Eddington luminosity (i.e. its luminosity is proportional to its mass). Therefore the cumulative emissivity of the first massive stars was proportional to their total cumulative mass, independent of their initial mass function. These stars produced $\sim 10^5$ ionizing photons per baryon incorporated into them [18, 99]. In comparison, low-mass stars produce $\sim 4,000$ ionizing photons per baryon [65]. In both cases, it is clear that only a small fraction of the baryons in the Universe needs to be converted into stars in order for them to ionize the rest.

Given the formation rate of galaxy halos as a function of cosmic time, the course of reionization can be determined by counting photons from all sources of light [4, 92, 112, 60, 44, 93, 48]. Both stars and black holes contribute ionizing photons, but the early Universe is dominated by small galaxies which in the local Universe have central black holes that are disproportionately small, and indeed quasars are rare above redshift 6 [35]. Thus, stars most likely dominated the production of ionizing UV photons during the reionization epoch [although high-redshift galaxies should have also emitted X-rays from accreting black holes and accelerated particles in collisionless shocks [81, 41]]. Since most stellar ionizing photons are only slightly more energetic than the 13.6 eV ionization threshold of hydrogen, they are absorbed efficiently once they reach a region with substantial neutral hydrogen. This makes the intergalactic medium (IGM) during reionization a two-phase medium characterized by highly ionized regions separated from neutral regions by sharp ionization fronts (see Figure 4).

We can obtain a first estimate of the requirements of reionization by demanding one stellar ionizing photon for each hydrogen atom in the IGM. If we conservatively assume that stars within the ionizing galaxies were similar to those observed locally, then each star produced ~ 4000 ionizing photons per baryon. Star formation is observed today to be an inefficient process, but even if stars in galaxies formed out of only $\sim 10\%$ of the available gas, it was still sufficient to accumulate a small fraction (of order 0.1%) of the total baryonic mass in the

Universe into galaxies in order to ionize the entire IGM. More accurate estimates of the actual required fraction account for the formation of some primordial stars (which were massive, efficient ionizers, as discussed above), and for recombinations of hydrogen atoms at high redshifts and in dense regions.

From studies of quasar absorption lines at $z \sim 6$ we know that the IGM is highly ionized a billion years after the Big Bang. There are hints, however, that some large neutral hydrogen regions persist at these early times [105, 74, 64] and so this suggests that we may not need to go to much higher redshifts to begin to see the epoch of reionization. We now know that the Universe could not have fully reionized earlier than an age of ~ 300 million years, since WMAP3 observed the effect of the freshly created plasma at reionization on the large-scale polarization anisotropies of the CMB and this limits the reionization redshift [100]; an earlier reionization, when the Universe was denser, would have created a stronger scattering signature that would be inconsistent with the WMAP3 observations. In any case, the redshift at which reionization ended only constrains the overall cosmic efficiency of ionizing photon production. In comparison, a detailed picture of reionization as it happens will teach us a great deal about the population of young galaxies that produced this cosmic phase transition.

Several quasars beyond $z \sim 6$ show in their spectra a Gunn-Peterson trough, a blank spectral region at wavelengths shorter than $\text{Ly}\alpha$ at the quasar redshift (Figure 3). The detection of Gunn-Peterson troughs indicates a rapid change [34, 102, 37] in the neutral content of the IGM at $z \sim 6$, and hence a rapid change in the intensity of the background ionizing flux. However, even a small atomic hydrogen fraction of $\sim 10^{-3}$ would still produce nearly complete $\text{Ly}\alpha$ absorption.

A key point is that the spatial distribution of ionized bubbles is determined by clustered groups of galaxies and not by individual galaxies. At such early times galaxies were strongly clustered even on very large scales (up to tens of Mpc), and these scales therefore dominated the structure of reionization [6]. The basic idea is simple [58]. At high redshift, galactic halos are rare and correspond to high density peaks. As an analogy, imagine searching on Earth for mountain peaks above 5000 meters. The 200 such peaks are not at all distributed uniformly but instead are found in a few distinct clusters on top of large mountain ranges. Given the large-scale boost provided by a mountain range, a small-scale crest need only provide a small additional rise in order to become a 5000 meter peak. The same crest, if it formed within a valley, would not come anywhere near 5000 meters in total height. Similarly, in order to find the early galaxies, one must first locate a region with a large-scale density enhancement, and then galaxies will be found there in abundance.

The ionizing radiation emitted from the stars in each galaxy initially produces an isolated ionized bubble. However, in a region dense with galaxies the bubbles quickly overlap into one large bubble, completing reionization in this region while the rest of the Universe is still mostly neutral (Figure 4). Most importantly, since the abundance of rare density peaks is very sensitive to small changes in the density threshold, even a large-scale region with a small enhanced density (say, 10% above the mean density of the Universe) can have a much larger concentration of galaxies than in other regions (e.g., a 50% enhancement). On the other hand, reionization is harder to achieve in dense regions, since the protons and electrons collide and recombine more often in such regions, and newly-formed hydrogen atoms need to be reionized again by additional ionizing photons. However, the overdense regions end up reionizing first since the number of ionizing sources in these regions is increased so strongly [6, 77]. The large-scale topology of reionization is therefore inside out, with underdense voids reionizing only at the very end of reionization, with the help of extra ionizing photons coming in from their surroundings (which have a higher density of galaxies than the voids themselves). This is a key prediction awaiting observational tests.

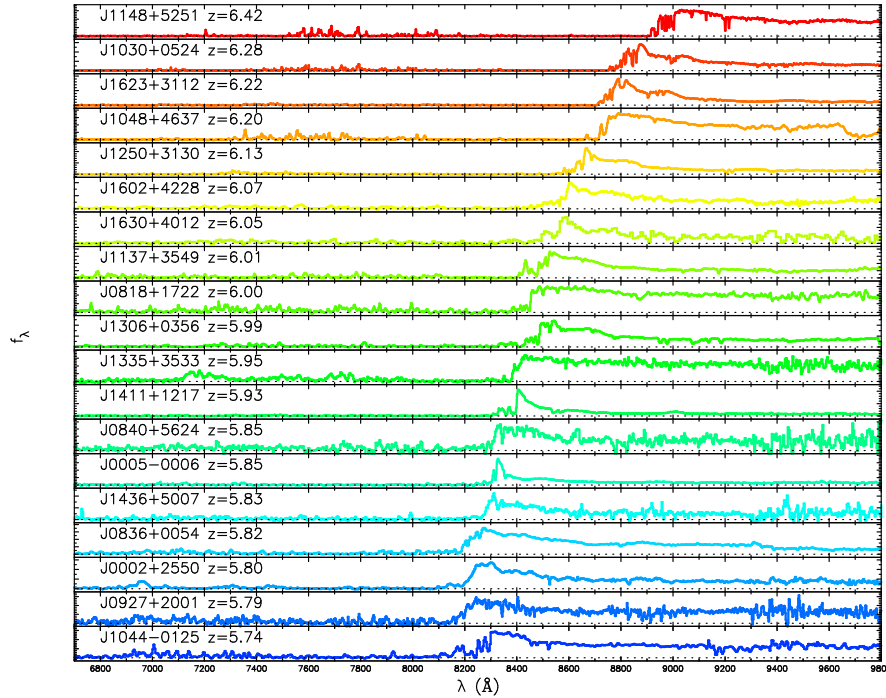


Fig. 3. Spectra of 19 quasars with redshifts $5.74 < z < 6.42$ from the *Sloan Digital Sky Survey*, taken from Fan et al. (2005). For some of the highest-redshift quasars, the spectrum shows no transmitted flux shortward of the $\text{Ly}\alpha$ wavelength at the quasar redshift (the so-called “Gunn-Peterson trough”), indicating a non-negligible neutral fraction in the IGM.

Detailed analytical models that account for large-scale variations in the abundance of galaxies [43] confirm that the typical bubble size starts well below a Mpc early in reionization, as expected for an individual galaxy, rises to 5–10 comoving Mpc during the central phase (i.e., when the Universe is half ionized), and then by another factor of ~ 5 towards the end of reionization. (These scales are given in comoving units that scale with the expansion of the Universe, so that the actual sizes at a redshift z were smaller than these numbers by a factor of $1+z$.) Numerical simulations have only recently begun to reach the enormous scales needed to capture this evolution [23, 73, 113]. Accounting precisely for gravitational evolution over a wide range of scales but still crudely for gas dynamics, star formation, and the radiative transfer of ionizing photons, the simulations confirm that the large-scale topology of reionization is inside out, and that this topology can be used to study the abundance and clustering of the ionizing sources (Figures 4 and 9).

Wyithe & Loeb (2004b) [106] showed that the characteristic size of the ionized bubbles at the end reionization can be calculated based on simple considerations that only depend on the power-spectrum of density fluctuations and the redshift. As the size of an ionized bubble increases, the time it takes a 21-cm photon to traverse it gets longer. At the same time, the variation in the time at which different regions reionize becomes smaller as the regions grow larger. Thus, there is a maximum size above which the photon crossing time is longer than

the cosmic variance in ionization time. Regions bigger than this size will be ionized at their near side by the time a 21-cm photon will cross them towards the observer from their far side. They would appear to the observer as one-sided, and hence signal the end of reionization. These “light cone” considerations imply a characteristic size for the ionized bubbles of ~ 10 physical Mpc at $z \sim 6$ (equivalent to 70 comoving Mpc). This result implies that future radio experiments should be tuned to a characteristic angular scale of tens of arcminutes and have a minimum frequency band-width of 5-10 MHz for an optimal detection of 21-cm brightness fluctuations near the end of reionization.

2.2 Simulations of Reionization

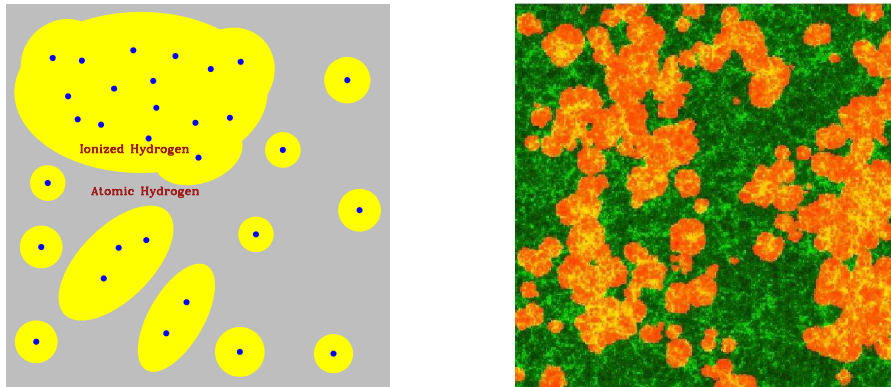


Fig. 4. The spatial structure of cosmic reionization. The illustration (left panel, based on Barkana & Loeb 2004b) shows how regions with large-scale overdensities form large concentrations of galaxies (dots) whose ionizing photons produce enormous joint ionized bubbles (upper left). At the same time, galaxies are rare within large-scale voids, in which the IGM is still mostly neutral (lower right). A numerical simulation of reionization (right panel, from Mellema et al. 2006) indeed displays such variation in the sizes of ionized bubbles (orange), shown overlaid on the density distribution (green).

Simulating reionization is challenging for two reasons. First, one needs to incorporate radiative transfer at multiple photon frequencies into a code that follows the dynamics of gas and dark matter. This implies that the sources of the radiation, i.e. galaxies, need to be resolved. Second, one needs to simulate a sufficiently large volume of the Universe for cosmic variance not to play a role [6]. Towards the end of reionization, the sizes of individual ionized regions grow up to a scale of ~ 50 – 100 comoving Mpc [106, 43] and the representative volume needs to include many such region in order for it to fully describe the large-scale topology of reionization. There is an obvious tension between the above two requirements for simulating small scales as well as large scales simultaneously.

Numerical simulations of reionization are starting to achieve the dynamic range required to resolve galaxy halos across the scale of hundreds of comoving Mpc, larger than the size of the ionized regions at the end of the reionization process [113, 56, 98]. These simulations cannot yet follow in detail the formation of individual stars within galaxies, or the feedback that

stars produce on the surrounding gas, such as photoheating or the hydrodynamic and chemical impact of supernovae, which blow hot bubbles of gas enriched with the chemical products of stellar nucleosynthesis. Thus, the simulations cannot directly predict whether the stars that form during reionization are similar to the stars in the Milky Way and nearby galaxies or to the primordial $100M_{\odot}$ behemoths. They also cannot determine whether feedback prevents low-mass dark matter halos from forming stars. Thus, models are needed that make it possible to vary all these astrophysical parameters of the ionizing sources.

3 Imaging Cosmic Hydrogen

3.1 Basic Principles

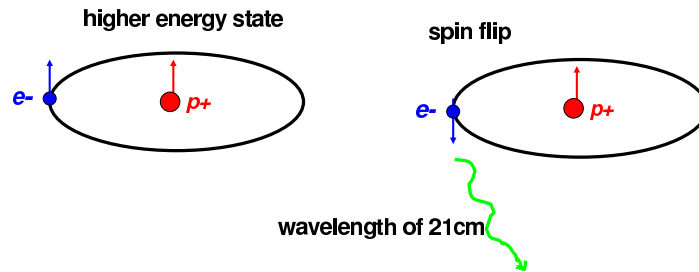


Fig. 5. The 21cm transition of hydrogen. The higher energy level the spin of the electron (e^-) is aligned with that of the proton (p^+). A spin flip results in the emission of a photon with a wavelength of 21cm (or a frequency of 1420MHz).

The ground state of hydrogen exhibits hyperfine splitting involving the spins of the proton and the electron. The state with parallel spins (the triplet state) has a slightly higher energy than the state with anti-parallel spins (the singlet state). The 21-cm line associated with the spin-flip transition from the triplet to the singlet state is often used to detect neutral hydrogen in the local Universe. At high redshift, the occurrence of a neutral pre-reionization intergalactic medium (IGM) offers the prospect of detecting the first sources of radiation and probing the reionization era by mapping the 21-cm absorption or emission from neutral regions. Regions

where the gas is slightly denser than the mean would produce a stronger signal. Therefore, the 21cm brightness will fluctuate across the sky as a result of the inhomogeneous distribution of hydrogen. Moreover, this resonant line can be used to slice the Universe at different redshifts z by observing different wavelengths corresponding to $21\text{cm}(1+z)$. Altogether, the 21cm brightness fluctuation can be used to map the inhomogeneous hydrogen distribution in three dimensions.

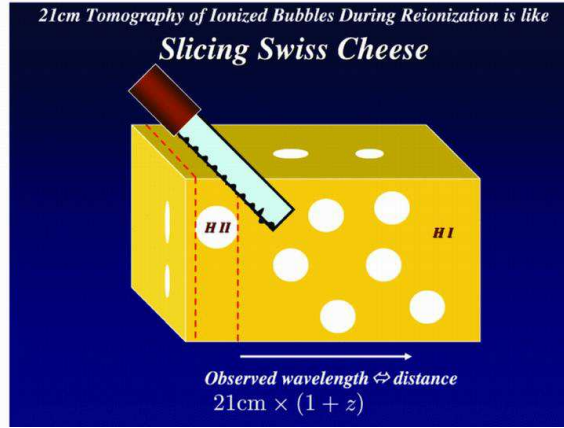


Fig. 6. 21cm imaging of ionized bubbles during the epoch of reionization is analogous to slicing swiss cheese. The technique of slicing at intervals separated by the typical dimension of a bubble is optimal for revealing different patterns in each slice.

The atomic hydrogen gas formed soon after the big-bang, was affected by processes ranging from quantum fluctuations during the early epoch of inflation to irradiation by the first galaxies at late times. Mapping this gas through its resonant 21cm line serves a dual role as a powerful probe of fundamental physics and of astrophysics. The facets of fundamental physics include the initial density fluctuations imprinted by inflation as well as the nature of the dark matter, which amplifies these fluctuations during the matter-dominated era. It is possible to avoid the contamination from astrophysical sources by observing the Universe before the first galaxies had formed. In the concordance Λ CDM cosmological model, the 21cm brightness fluctuations of hydrogen were shaped by fundamental physics (inflation, dark matter, and atomic physics) at redshifts $z > 20$, and by the radiation from galaxies at lower redshifts.

Following cosmological recombination at $z \sim 10^3$, the residual fraction of free electrons coupled the gas thermally to the cosmic microwave background (CMB) for another 65 million years ($z \sim 200$), but afterwards the gas decoupled and cooled faster than the CMB through its cosmic expansion. In the redshift interval of the so-called *Dark Ages* before the first stars had formed, $30 < z < 200$, the *spin temperature* of hydrogen, T_s (defined through the level population of the spin-flip transition), was lower than the CMB temperature, T_γ , and the gas appeared in absorption. The primordial inhomogeneities of the gas produced varying levels of 21cm absorption and hence brightness fluctuations. Detection of this signal can be used to constrain models of inflation as well as the nature of dark matter [53, 89, 68, 63]. Altogether, there are $\sim 10^{16}$ independent pixels on the 21cm sky from this epoch (instead of $\sim 10^7$ for the

CMB). They make the richest data set on the sky, providing an unprecedented probe of non-Gaussianity and running of the spectral index of the power-spectrum of primordial density fluctuations from inflation. Detection of these small-scale fluctuations can also be used to infer the existence of massive neutrinos and other sub-dominant components in addition to the commonly inferred cold dark matter particles.

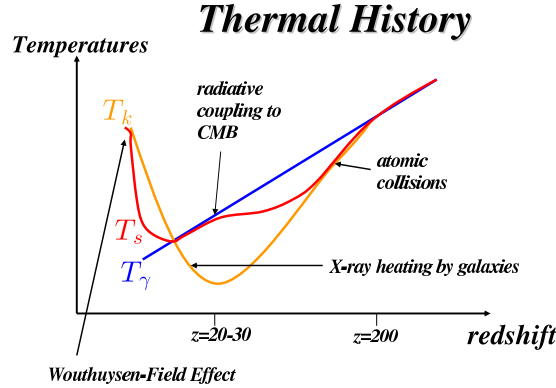


Fig. 7. Schematic sketch of the evolution of the kinetic temperature (T_k) and spin temperature (T_s) of cosmic hydrogen (from Loeb 2006). Following cosmological recombination at $z \sim 10^3$, the gas temperature (orange curve) tracks the CMB temperature (blue line; $T_\gamma \propto (1+z)$) down to $z \sim 200$ and then declines below it ($T_k \propto (1+z)^2$) until the first X-ray sources (accreting black holes or exploding supernovae) heat it up well above the CMB temperature. The spin temperature of the 21cm transition (red curve) interpolates between the gas and CMB temperatures. Initially it tracks the gas temperature through collisional coupling; then it tracks the CMB through radiative coupling; and eventually it tracks the gas temperature once again after the production of a cosmic background of UV photons between the Ly α and the Lyman-limit frequencies that redshift or cascade into the Ly α resonance (through the Wouthuysen-Field effect [101, 39]). Parts of the curve are exaggerated for pedagogical purposes. The exact shape depends on astrophysical details about the first galaxies, such as the production of X-ray binaries, supernovae, nuclear accreting black holes, and the generation of relativistic electrons in collisionless shocks which produce UV and X-ray photons through inverse-Compton scattering of CMB photons.

After the first galaxies formed and X-ray sources heated the gas above the CMB temperature, the gas appeared in 21cm emission. The bubbles of ionized hydrogen around groups of galaxies were dark and dominated the 21cm fluctuations [42, 83]. After the first stars had formed, the 21cm fluctuations were sourced mainly by the hydrogen ionized fraction, and spin temperature [70].

The basic physics of the hydrogen spin transition is determined as follows (for a more detailed treatment, see Refs. [70, 42]). The ground-state hyperfine levels of hydrogen tend to thermalize with the CMB bringing the IGM away from thermal equilibrium, then the gas becomes observable against the CMB in emission or in absorption. The relative occupancy of the spin levels is described in terms of the hydrogen spin temperature T_S , defined through the Boltzman factor,

$$\frac{n_1}{n_0} = 3 \exp \left\{ -\frac{T_*}{T_S} \right\}, \quad (1)$$

where n_0 and n_1 refer respectively to the singlet and triplet hyperfine levels in the atomic ground state ($n = 1$), and $T_* = 0.068$ K is defined by $k_B T_* = E_{21}$, where the energy of the 21 cm transition is $E_{21} = 5.9 \times 10^{-6}$ eV, corresponding to a frequency of 1420 MHz. In the presence of the CMB alone, the spin states reach thermal equilibrium with the CMB temperature $T_S = T_\gamma = 2.725(1+z)$ K on a time-scale of $T_*/(T_\gamma A_{10}) \simeq 3 \times 10^5 (1+z)^{-1}$ yr, where $A_{10} = 2.87 \times 10^{-15} \text{ s}^{-1}$ is the spontaneous decay rate of the hyperfine transition. This time-scale is much shorter than the age of the Universe at all redshifts after cosmological recombination.

The IGM is observable when the kinetic temperature T_k of the gas differs from the CMB temperature T_γ and an effective mechanism couples T_S to T_k . Collisional de-excitation of the triplet level [86] dominates at very high redshift, when the gas density (and thus the collision rate) is still high, making the gas observable in absorption. Once a significant galaxy population forms in the Universe, the X-rays they emit heat T_k above T_γ and the UV photons they emit couple T_S to T_k making the gas appear in 21cm emission. The latter coupling mechanism acts through the scattering of Ly α photons [101, 39]. Continuum UV photons produced by early radiation sources redshift by the Hubble expansion into the local Ly α line at a lower redshift. These photons mix the spin states via the Wouthuysen-Field process whereby an atom initially in the $n = 1$ state absorbs a Ly α photon, and the spontaneous decay which returns it from $n = 2$ to $n = 1$ can result in a final spin state which is different from the initial one. Since the neutral IGM is highly opaque to resonant scattering, and the Ly α photons receive Doppler kicks in each scattering, the shape of the radiation spectrum near Ly α is determined by T_k [39], and the resulting spin temperature (assuming $T_S \gg T_*$) is then a weighted average of T_k and T_γ :

$$T_S = \frac{T_\gamma T_k (1 + x_{\text{tot}})}{T_k + T_\gamma x_{\text{tot}}}, \quad (2)$$

where $x_{\text{tot}} = x_\alpha + x_c$ is the sum of the radiative and collisional threshold parameters. These parameters are $x_\alpha = \frac{P_{10} T_\gamma}{A_{10} T_\gamma}$, and $x_c = \frac{4\kappa_{1-0}(T_k) n_H T_*}{3A_{10} T_\gamma}$, where P_{10} is the indirect de-excitation rate of the triplet $n = 1$ state via the Wouthuysen-Field process, related to the total scattering rate P_α of Ly α photons by $P_{10} = 4P_\alpha/27$ [38]. Also, the atomic coefficient $\kappa_{1-0}(T_k)$ is tabulated as a function of T_k [2, 115]. Note that we have adopted the modified notation (i.e., in terms of x_α and x_c) of Barkana & Loeb (2005b) [8]. The coupling of the spin temperature to the gas temperature becomes substantial when $x_{\text{tot}} > 1$; in particular, $x_\alpha = 1$ defines the thermalization rate [70] of P_α : $P_{\text{th}} \equiv \frac{27A_{10} T_\gamma}{4T_*} \simeq 7.6 \times 10^{-12} \left(\frac{1+z}{10}\right) \text{ s}^{-1}$.

A patch of neutral hydrogen at the mean density and with a uniform T_S produces (after correcting for stimulated emission) an optical depth at a present-day (observed) wavelength of $21(1+z)$ cm,

$$\tau(z) = 9.0 \times 10^{-3} \left(\frac{T_\gamma}{T_S}\right) \left(\frac{\Omega_b h}{0.03}\right) \left(\frac{\Omega_m}{0.3}\right)^{-1/2} \left(\frac{1+z}{10}\right)^{1/2}, \quad (3)$$

assuming a high redshift $z \gg 1$. The observed spectral intensity I_ν relative to the CMB at a frequency ν is measured by radio astronomers as an effective brightness temperature T_b of

blackbody emission at this frequency, defined using the Rayleigh-Jeans limit of the Planck radiation formula: $I_\nu \equiv 2k_B T_b \nu^2 / c^2$.

The brightness temperature through the IGM is $T_b = T_\gamma e^{-\tau} + T_S(1 - e^{-\tau})$, so the observed differential antenna temperature of this region relative to the CMB is [70]

$$T_b = (1+z)^{-1}(T_S - T_\gamma)(1 - e^{-\tau}) \\ \simeq 28 \text{ mK} \left(\frac{\Omega_b h}{0.033} \right) \left(\frac{\Omega_m}{0.27} \right)^{-1/2} \left(\frac{1+z}{10} \right)^{1/2} \left(\frac{T_S - T_\gamma}{T_S} \right), \quad (4)$$

where $\tau \ll 1$ can be assumed and T_b has been redshifted to redshift zero. Note that the combination that appears in T_b is $\frac{T_S - T_\gamma}{T_S} = \frac{x_{\text{tot}}}{1+x_{\text{tot}}} \left(1 - \frac{T_\gamma}{T_S} \right)$. In overdense regions, the observed T_b is proportional to the overdensity, and in partially ionized regions T_b is proportional to the neutral fraction. Also, if $T_S \gg T_\gamma$ then the IGM is observed in emission at a level that is independent of T_S . On the other hand, if $T_S \ll T_\gamma$ then the IGM is observed in absorption at a level that is enhanced by a factor of T_γ/T_S .

To complement computationally-intensive simulations of reionization, various groups developed approximate schemes for simulating 21-cm maps in the regime where T_S is much larger than T_γ . For example, Furlanetto et al. (2004) [43] developed an analytical model that allows the calculation of the probability distribution (at a given redshift) of the size of the ionizing bubble surrounding a random point in space. Zahn et al. (2006) [113] have considered numerical schemes that apply the Furlanetto et al. (2004) model to either the initial conditions of their simulation or to part of its results (Figure 10).

3.2 Predicted 21cm Signal

In approaching redshifted 21-cm observations, although the first inkling might be to consider the mean emission signal, the signal is orders of magnitude fainter than foreground synchrotron emission from relativistic electrons in the magnetic field of our own Milky Way [42] as well as other galaxies [27]. Thus cosmologists have focused on the expected characteristic variations in T_b , both with position on the sky and especially with frequency, which signifies redshift for the cosmic signal. The synchrotron foreground is expected to have a smooth frequency spectrum, and so it is possible to isolate the cosmological signal by taking the difference in the sky brightness fluctuations at slightly different frequencies (as long as the frequency separation corresponds to the characteristic size of ionized bubbles). The 21-cm brightness temperature depends on the density of neutral hydrogen. As explained in the previous subsection, large-scale patterns in the reionization are driven by spatial variations in the abundance of galaxies; the 21-cm fluctuations reach ~ 5 mK (root mean square) in brightness temperature (Figure 9) on a scale of 10 comoving Mpc. While detailed maps will be difficult to extract due to the foreground emission, a statistical detection of these fluctuations (through the power spectrum) is expected to be well within the capabilities of the first-generation experiments now being built [17, 76]. Current work suggests that the key information on the topology and timing of reionization can be extracted statistically (Fig. 8).

The theoretical expectations for reionization and for the 21-cm signal are based on rather large extrapolations from observed galaxies to deduce the properties of much smaller galaxies that formed at an earlier cosmic epoch. Considerable surprises are thus possible, such as an early population of quasars or even unstable exotic particles that emitted ionizing radiation as they decayed.

An important cross-check on these measurements is possible by measuring the particular form of anisotropy, expected in the 21-cm fluctuations, that is caused by gas motions along

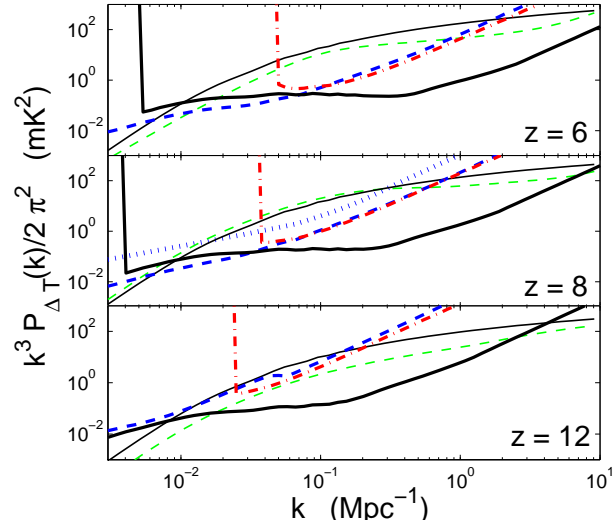


Fig. 8. Detectability of the power-spectrum of 21cm fluctuations by different future observatories (from McQuinn et al. 2006). The detector noise plus sample variance errors is shown for a 1000 hr observation on a single field in the sky, assuming perfect foreground removal, for MWA (*thick dashed curve*), LOFAR (*thick dot-dashed curve*), and SKA (*thick solid curve*) for wavenumber bins of $\Delta k = 0.5k$. The thin solid curve represents the spherically averaged signal for a small ionization fraction and $T_s \gg T_\gamma$.

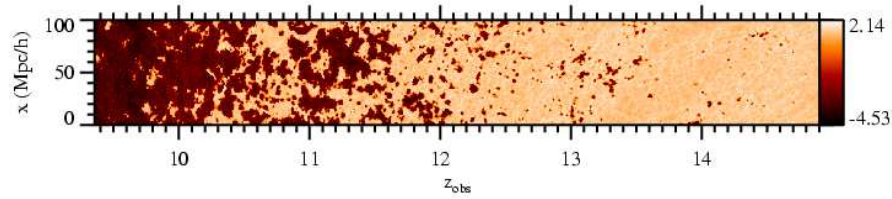


Fig. 9. Close-up of cosmic evolution during the epoch of reionization, as revealed in a predicted 21-cm map of the IGM based on a numerical simulation (from Mellema et al. 2006). This map is constructed from slices of the simulated cubic box of side 150 Mpc (in comoving units), taken at various times during reionization, which for the parameters of this particular simulation spans a period of 250 million years from redshift 15 down to 9.3. The vertical axis shows position χ in units of Mpc/h (where the Hubble constant in units of 100 km s^{-1} is $h = 0.7$). This two-dimensional slice of the sky (one linear direction on the sky versus the line-of-sight or redshift direction) shows $\log_{10}(T_b)$, where T_b (in mK) is the 21-cm brightness temperature relative to the CMB. Since neutral regions correspond to strong emission (i.e., a high T_b), this slice illustrates the global progress of reionization and the substantial large-scale spatial fluctuations in reionization history. Observationally it corresponds to a narrow strip half a degree in length on the sky observed with radio telescopes over a wavelength range of 2.2 to 3.4 m (with each wavelength corresponding to 21-cm emission at a specific line-of-sight distance and redshift).

the line of sight [59, 12, 7]. This anisotropy, expected in any measurement of density that is based on a spectral resonance or on redshift measurements, results from velocity compression. Consider a photon traveling along the line of sight that resonates with absorbing atoms at a particular point. In a uniform, expanding Universe, the absorption optical depth encountered by this photon probes only a narrow strip of atoms, since the expansion of the Universe makes all other atoms move with a relative velocity that takes them outside the narrow frequency width of the resonance line. If there is a density peak, however, near the resonating position, the increased gravity will reduce the expansion velocities around this point and bring more gas into the resonating velocity width. This effect is sensitive only to the line-of-sight component of the velocity gradient of the gas, and thus causes an observed anisotropy in the power spectrum even when all physical causes of the fluctuations are statistically isotropic. Barkana & Loeb (2005a) showed that this anisotropy is particularly important in the case of 21-cm fluctuations. When all fluctuations are linear, the 21-cm power spectrum takes the form [7] $P_{21\text{-cm}}(\mathbf{k}) = \mu^4 P_\rho(k) + 2\mu^2 P_{\rho\text{-iso}}(k) + P_{\text{iso}}$, where $\mu = \cos\theta$ in terms of the angle θ between the wavevector \mathbf{k} of a given Fourier mode and the line of sight, P_{iso} is the isotropic power spectrum that would result from all sources of 21-cm fluctuations without velocity compression, $P_\rho(k)$ is the 21-cm power spectrum from gas density fluctuations alone, and $P_{\rho\text{-iso}}(k)$ is the Fourier transform of the cross-correlation between the density and all sources of 21-cm fluctuations. The three power spectra can also be denoted $P_{\mu^4}(k)$, $P_{\mu^2}(k)$, and $P_{\mu^0}(k)$, according to the power of μ that multiplies each term. At these redshifts, the 21-cm fluctuations probe the infall of the baryons into the dark matter potential wells [9]. The power spectrum shows remnants of the photon-baryon acoustic oscillations on large scales, and of the baryon pressure suppression on small scales [80].

Once stellar radiation becomes significant, many processes can contribute to the 21-cm fluctuations. The contributions include fluctuations in gas density, temperature, ionized fraction, and Ly α flux. These processes can be divided into two broad categories: The first, related to “*physics*”, consists of probes of fundamental, precision cosmology, and the second, related to “*astrophysics*”, consists of probes of stars. Both categories are interesting – the first for precision measures of cosmological parameters and studies of processes in the early Universe, and the second for studies of the properties of the first galaxies. However, the astrophysics depends on complex non-linear processes (collapse of dark matter halos, star formation, supernova feedback), and must be cleanly separated from the physics contribution, in order to allow precision measurements of the latter. As long as all the fluctuations are linear, the anisotropy noted above allows precisely this separation of the physics from the astrophysics of the 21-cm fluctuations [7]. In particular, the $P_{\mu^4}(k)$ is independent of the effects of stellar radiation, and is a clean probe of the gas density fluctuations. Once non-linear terms become important, there arises a significant mixing of the different terms; in particular, this occurs on the scale of the ionizing bubbles during reionization [76].

At early times, the 21-cm fluctuations are also affected by fluctuations in the Ly α flux from stars, a result that yields an indirect method to detect and study the early population of galaxies at $z \sim 20$ [8]. The fluctuations are caused by biased inhomogeneities in the density of galaxies, along with Poisson fluctuations in the number of galaxies. Observing the power-spectra of these two sources would probe the number density of the earliest galaxies and the typical mass of their host dark matter halos. Furthermore, the enhanced amplitude of the 21cm fluctuations from the era of Ly α coupling improves considerably the practical prospects for their detection. Precise predictions account for the detailed properties of all possible cascades of a hydrogen atom after it absorbs a photon [52, 82]. Around the same time, X-rays may also start to heat the cosmic gas, producing strong 21-cm fluctuations due to fluctuations in the X-ray flux [83].

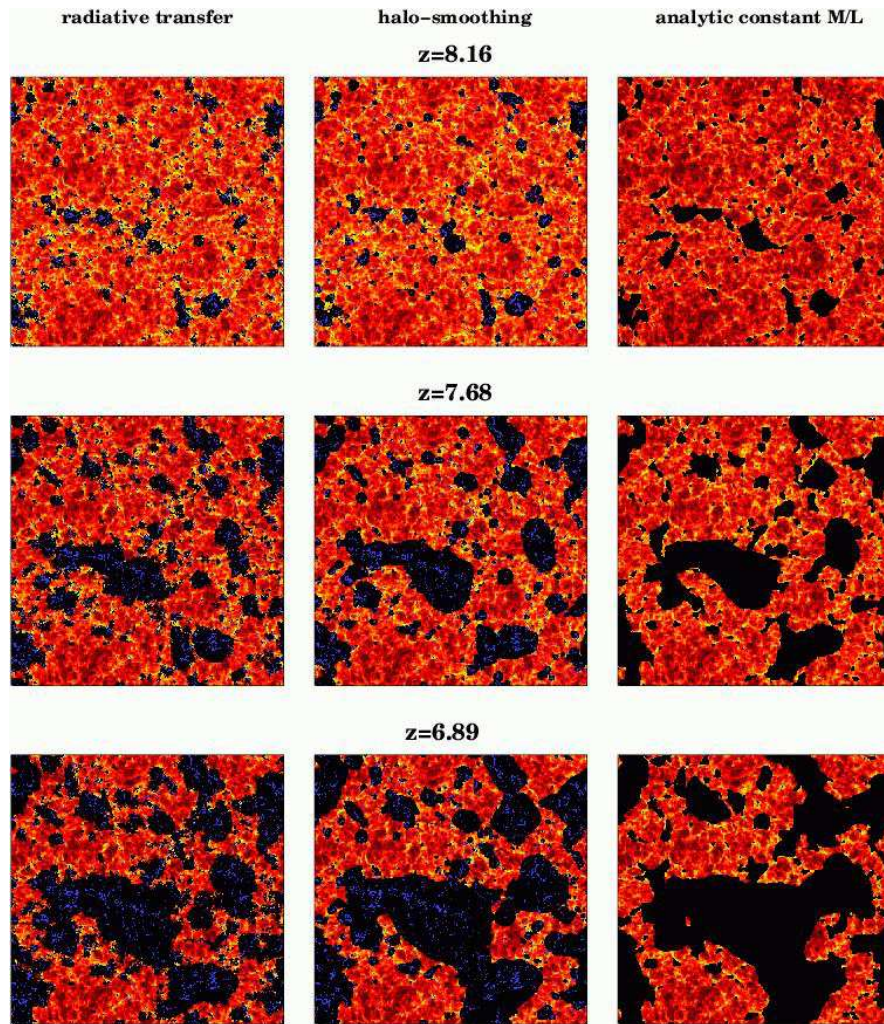


Fig. 10. Maps of the 21-cm brightness temperature comparing results of a numerical simulation and of two simpler numerical schemes, at three different redshifts (from Zahn et al. 2006). Each map is $65.6 \text{ Mpc}/h$ on a side, with a depth ($0.25 \text{ Mpc}/h$) that is comparable to the frequency resolution of planned experiments. The ionized fractions are $x_i = 0.13, 0.35$ and 0.55 for $z = 8.16, 7.26$ and 6.89 , respectively. All three maps show a very similar large-scale ionization topology. *Left column:* Numerical simulation, showing the ionized bubbles (black) produced by the ionizing sources (blue dots) that form in the simulation. *Middle column:* Numerical scheme that applies the Furlanetto et al. (2004) analytical model to the final distribution of ionizing sources that form in the simulation. *Right column:* Numerical scheme that applies the Furlanetto et al. (2004) analytical model to the linear density fluctuations that are the initial conditions of the simulation.

3.3 Baryonic Acoustic Oscillation

As described above, the fluctuations in the emission of redshifted 21cm photons from neutral intergalactic hydrogen will provide an unprecedented probe of the reionization era. Conventional wisdom assumes that this 21cm signal disappears as soon as reionization is complete, when little atomic hydrogen is left through most of the volume of the IGM. However, the statistics of damped Ly α absorbers (DLAs) in quasar spectra indicate that a few percent of the baryonic mass reservoir remains in the form of atomic hydrogen at all redshifts. The residual hydrogen is self-shielded from UV radiation within dense regions in which the recombination rate is high. Wyithe & Loeb (2007) used a physically-motivated model to show that residual neutral gas would generate a significant post-reionization 21cm signal. Even though the signal is much weaker (see Fig. 11) than that of a fully-neutral IGM, the synchrotron foreground, whose brightness temperature scales as $\propto (1+z)^{2.6}$, is also much weaker at the corresponding low redshifts. Thus, the power-spectrum of fluctuations in this signal will be detectable by the first generation of low-frequency observatories at a signal-to-noise that is comparable to that achievable in observations of the reionization era. The statistics of 21cm fluctuations will therefore probe not only the pre-reionization IGM, but rather the entire process of HII region overlap, as well as the appearance of the diffuse ionized IGM. With an angular resolution of an arcminute, the radio beam of future interferometers will contain many DLAs and will not resolve them individually. Rather, the observations will map the course-binned distribution of neutral hydrogen across scales of tens of comoving Mpc.

Wyithe, Loeb, & Geil (2007) demonstrated that the power spectrum of the cumulative 21cm emission during and after reionization will show baryonic acoustic oscillations (BAOs), whose comoving scale can be used as a standard ruler to infer the evolution of the equation of state for the dark energy. The BAO yardstick can be used to measure the dependence of both the angular diameter distance and Hubble parameter on redshift. The wavelength of the BAO is related to the size of the sound horizon at recombination, as this reflects the distance out to which different points were correlated in the radiation-baryon fluid. Its value depends on the Hubble constant and on the matter and baryon densities. However, it does not depend on the amount or nature of the dark energy. Thus, measurements of the angular diameter distance and Hubble parameter can in turn be used to constrain the possible evolution of the dark energy with cosmic time. This idea was originally proposed in relation to galaxy redshift surveys [13, 55, 90] and has since received significant theoretical attention [47, 91, 3]. Moreover, measurement of the BAO scale has been achieved within large surveys of galaxies at low redshift, illustrating its potential [24, 32]. Galaxy redshift surveys are best suited to studies of the dark energy at relatively late times due to the difficulty of obtaining accurate redshifts for large numbers of high redshift galaxies. Wyithe, Loeb, & Geil (2007) have found that the first generation of low-frequency experiments (such as MWA or LOFAR) will be able to constrain the acoustic scale to within a few percent in a redshift window just prior to the end of the reionization era. This sensitivity to the acoustic scale is comparable to the best current measurements from galaxy redshift surveys, but at much higher redshifts. Future extensions of the first generation experiments (involving an order of magnitude increase in the antennae number of the MWA) could reach sensitivities below one percent in several redshift windows and could be used to study the dark energy in the unexplored redshift regime of $3.5 < z < 12$. Moreover, new experiments with antennae designed to operate at higher frequencies would allow precision measurements ($< 1\%$) of the acoustic peak to be made at more moderate redshifts ($1.5 < z < 3.5$), where they would be competitive with ambitious spectroscopic galaxy surveys covering more than 1000 square degrees. Together with other data sets, observations

of 21cm fluctuations will allow full coverage of the acoustic scale from the present time out to $z \sim 12$ [111] and beyond [9].

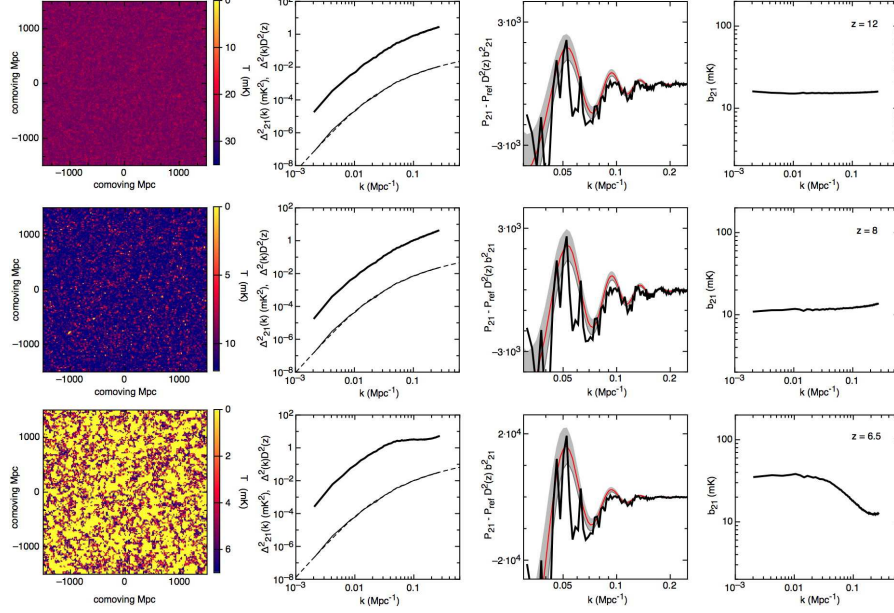


Fig. 11. Examples of the 21cm power spectra during reionization (from Wyithe, Loeb, & Geil 2007). *Left panels:* Maps of the 21cm emission from slices through the numerical simulation boxes, each 3000 co-moving Mpc on a side with a thickness of 12 co-moving Mpc. In these maps yellow designates the absence of redshifted 21cm emission. *Central-left panels:* The corresponding matter power spectra multiplied by the growth factor squared (thin solid lines) as well as the 21cm (thick solid lines) power spectra computed from the simulation box. The input co-moving power spectrum P (also multiplied by the growth factor squared) is shown for comparison (short-dashed lines). *Central-right panels:* The baryonic oscillations component of the simulated 21cm power spectrum. The curves (thick dark lines) show the difference between the simulated 21cm power spectrum, and a reference no wiggle 21cm power spectrum computed from the theoretical no wiggle reference matter power spectrum multiplied by the square of the product between the bias and the growth factor [i.e. $P_{21} - P_{\text{ref}} b_{21}^2 D^2$]. For comparison, the red lines show the difference between the input matter and the no-BAO reference matter power spectra, multiplied by the bias and growth factor squared [i.e. $(P - P_{\text{ref}}) b_{21}^2 D^2$]. The grey band surrounding this curve shows the level of statistical scatter in realizations of the power spectrum due to the finite size of the simulation volume. *Right panels:* The scale dependent bias (b_{21}). The upper, central and lower panels show results at $z = 12$, $z = 8$ and $z = 6.5$, which have global neutral fractions of 98%, 48% and 11% respectively in the model shown.

The left hand panels of Figure 11 show the 21cm emission from 12Mpc slices through a numerical simulation [111]. The higher redshift example ($z = 12$) is early in the reionization era, and shows no HII regions forming at the resolution of the simulation (i.e. the IGM does

not contain ionized bubbles with radii > 5 co-moving Mpc). The fluctuations in the 21cm emission are dominated by the density field at this time. The central redshift ($z \sim 8$) shows the IGM midway through the reionization process, and includes a few HII regions above the simulation resolution. The lower redshift example is just prior to the overlap of the ionized regions (and hence the completion of reionization), when the IGM is dominated by large percolating HII regions.

3.4 Low-Frequency Arrays

The main obstacle towards detecting the 21cm signal is the synchrotron foreground contamination from our Galaxy and extragalactic point sources, whose brightness temperature rises steeply towards lower frequencies ($\propto \nu^{-2.6}$) and makes the detection of the redshifted 21cm line more challenging at higher redshifts. This fact directed most experimental and theoretical work so far towards the study of the astrophysics-dominated era at low redshifts ($z < 20$), during which the 21cm fluctuations were sourced mainly by the growth of ionized bubbles around galaxies. For example, the Murchison Wide-Field Array (MWA; Fig. 12), which is currently funded by NSF and the Australian government, is designed to cover the redshift range of 6–17. The first generation MWA-demonstrator will have 512 antenna tiles of 4×4 dipole antennae each.



Fig. 12. Prototype of the tile design for the *Murchison Wide-Field Array* (MWA) in western Australia, aimed at detecting redshifted 21cm from the epoch of reionization. Each $4\text{m} \times 4\text{m}$ tile contains 16 dipole antennas operating in the frequency range of 80–300MHz. Altogether the initial phase of MWA (the so-called “Low-Frequency Demonstrator”) will include 500 antenna tiles with a total collecting area of 8000 m^2 at 150MHz, scattered across a 1.5 km region and providing an angular resolution of a few arcminutes.

The prospect of studying reionization by mapping the distribution of atomic hydrogen across the Universe using its prominent 21-cm spectral line has motivated several teams to

design and construct arrays of low-frequency radio telescopes; the Low Frequency Array¹, MWA², the 21CMA³, and ultimately the Square Kilometer Array⁴ will search over the next decade for 21-cm emission or absorption from $z \sim 3.5\text{--}15$, redshifted and observed today at relatively low frequencies which correspond to wavelengths of 1 to 4 meters. Producing resolved images even of large sources such as cosmological ionized bubbles requires telescopes which have a kilometer scale. It is much more cost-effective to use a large array of thousands of simple antennas distributed over several kilometers, and to use computers to cross-correlate the measurements of the individual antennas and combine them effectively into a single large telescope. The new experiments are being placed mostly in remote sites, because the cosmic wavelength region overlaps with more mundane terrestrial telecommunications.

4 Imaging Galaxies

4.1 Future Infrared Telescopes

Narrow-band searches for redshifted Ly α emission have discovered galaxies robustly out to redshifts $z = 6.96$ [57] and potentially out to $z = 10$ [94]. Existing observations provide a first glimpse into the formation of the first galaxies [71, 61, 96, 28] with potential theoretical implications for the epoch of reionization [67, 87, 49, 72, 95, 77, 75]. Future surveys intend to exploit this search strategy further by pushing to even higher redshifts and fainter flux levels [54, 103, 104, 25]. The spectral break due to Ly α absorption by the IGM allows to identify high-redshift galaxies photometrically with even greater sensitivity [14, 15, 31] (see overview in Ref. [33] and phenomenological model in Ref. [95]).

The construction of large infrared telescopes on the ground and in space will provide us with new photos of first generation of galaxies during the epoch of reionization. Current plans include the space telescope JWST (which will not be affected by the atmospheric background) as well as ground-based telescopes which are 24-42 meter in diameter (such as the GMT⁵, TMT⁶, and EELT⁷).

4.2 Cross-Correlating Galaxies with 21cm Maps

Given that the earliest galaxies created the ionized bubbles around them by their UV emission, the locations of galaxies should correlate with the cavities in the neutral hydrogen during reionization. Within a decade it should be possible to explore the environmental influence of individual galaxies by using large-aperture infrared telescopes in combination with 21-cm observatories of reionization [108, 107, 110].

Wyithe & Loeb (2007) [108] calculated the expected anti-correlation between the distribution of galaxies and the intergalactic 21cm emission at high redshifts. As already mentioned, overdense regions are expected to be ionized first as a result of their biased galaxy formation.

¹ <http://www.lofar.org/>

² <http://www.haystack.mit.edu/ast/arrays/mwa/index.html>

³ <http://arxiv.org/abs/astro-ph/0502029>

⁴ <http://www.skatelescope.org>

⁵ <http://www.gmto.org/>

⁶ <http://celt.ucoick.org/>

⁷ <http://www.eso.org/projects/e-elt/>



Fig. 13. Artist's conception of the design for one of the future giant telescopes that could probe the first generation of galaxies from the ground. The *Giant Magellan Telescope (GMT)* will contain seven mirrors (each 8.4 meter in diameter) and will have a resolving power equivalent to a 24.5 meter (80 foot) primary mirror. For more details see <http://www.gmto.org/>.

This early phase leads to an anti-correlation between the 21cm emission and the overdensity in galaxies, matter, or neutral hydrogen. Existing $\text{Ly}\alpha$ surveys probe galaxies that are highly clustered in overdense regions. By comparing 21cm emission from regions near observed galaxies to those away from observed galaxies, future observations will be able to test this generic prediction and calibrate the ionizing luminosity of high-redshift galaxies. McQuinn et al. (2007a) [78] showed that observations of high-redshift Ly-alpha emitters (LAEs) have the potential to provide definitive evidence for reionization because their $\text{Ly}\alpha$ line is damped by the neutral regions in the IGM. In particular, the clustering of the emitters is increased by incomplete reionization (Fig. 14). For stellar reionization scenarios, the angular correlation function of the 58 LAEs in the Subaru Deep Field $z = 6.6$ photometric sample [96, 61] is already consistent with a mostly ionized IGM [78]. At higher redshifts near the beginning of reionization, when the ionized regions were small, this analysis needs to be combined with detailed radiative transfer calculations of the $\text{Ly}\alpha$ line, since the line shape is sensitive to the local infall/outflow profile of the gas around individual galaxies [29].

4.3 Gamma-ray Bursts: Probing the First Stars One Star at a Time

Gamma-Ray Bursts (GRBs) are believed to originate in compact remnants (neutron stars or black holes) of massive stars. Their high luminosities make them detectable out to the edge of the visible Universe [62, 26]. GRBs offer the opportunity to detect the most distant (and hence earliest) population of massive stars, the so-called Population III (or Pop III), one star at a time (Figure 15). In the hierarchical assembly process of halos that are dominated by cold dark matter, the first galaxies should have had lower masses (and lower stellar luminosities) than their

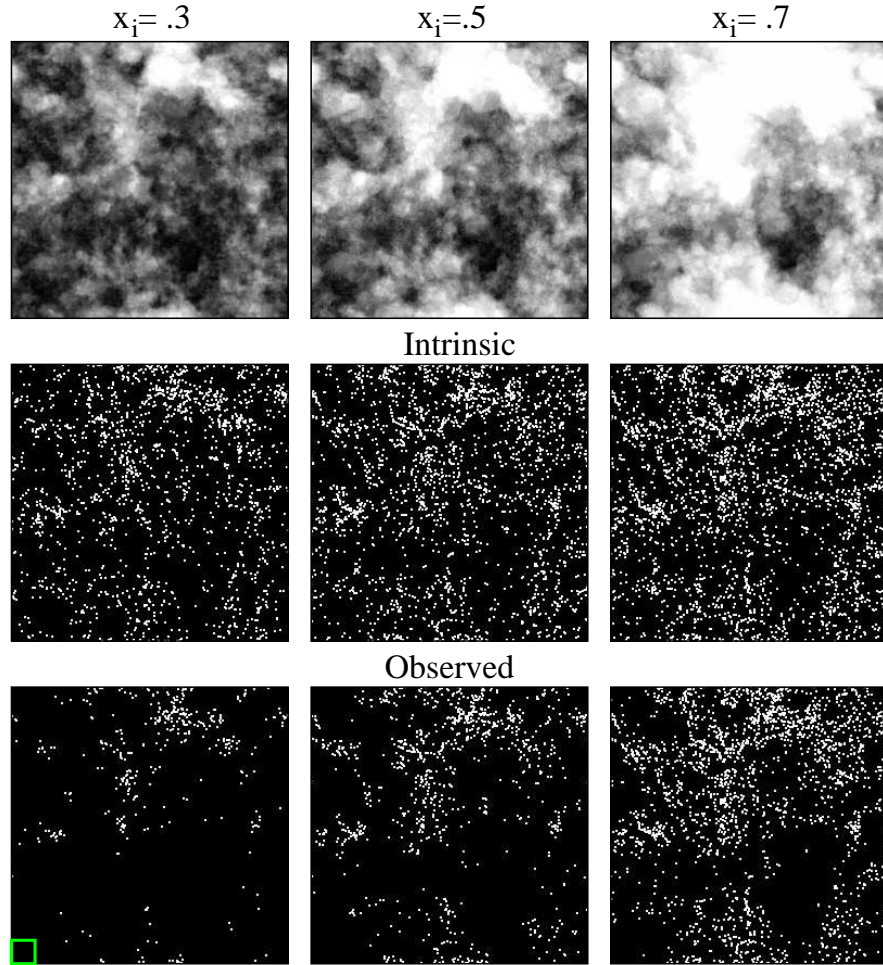


Fig. 14. Simulation results (from McQuinn et al. 2007a[78]) for the relative distribution of neutral hydrogen and Ly α emitting galaxies (LAE). The top panels show the projection of the ionized hydrogen fraction x_i in the survey volume. In the white regions the projection is fully ionized and in black it is neutral. The left, middle, and right panels are for $z = 8.2$ (with an average ionized fraction $\bar{x}_i = 0.3$), $z = 7.7$ ($\bar{x}_i = 0.5$), and $z = 7.3$ ($\bar{x}_i = 0.7$). The middle and bottom rows are the intrinsic and observed LAE maps, respectively, for a futuristic LAE survey that can detect halos down to a mass $> 1 \times 10^{10} M_\odot$. The observed distribution of emitters is modulated by the location of the HII regions (compare bottom panels with corresponding top panels). Each panel is 94 comoving Mpc across (or 0.6 degrees on the sky), roughly the area of the current Subaru Deep Field (SDF) at $z = 6.6$ [61]. The depth of each panel is $\Delta\lambda = 130\text{\AA}$, which matches the FWHM of the Subaru 9210 \AA narrow-band filter. The number densities of LAEs for the panels in the middle row are few times larger than the number density in the SDF photometric sample of $z = 6.6$ LAEs. The large-scale modulation of LAE by the HII bubbles is clearly apparent in this survey. The square in the lower left-hand panel represents the $3' \times 3'$ field-of-view of *JWST* drawn to scale.

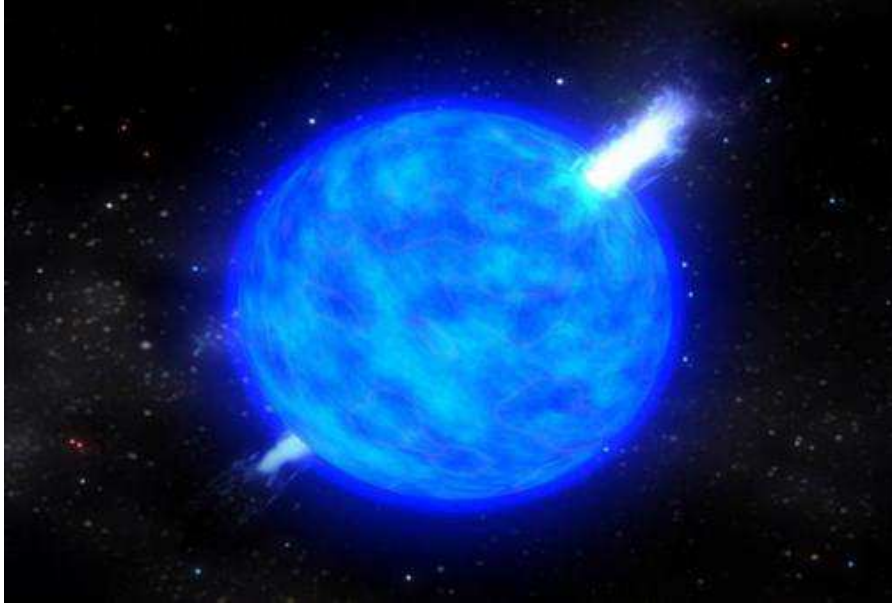


Fig. 15. Illustration of a long-duration gamma-ray burst in the popular “collapsar” model [114]. The collapse of the core of a massive star (which lost its hydrogen envelope) to a black hole generates two opposite jets moving out at a speed close to the speed of light. The jets drill a hole in the star and shine brightly towards an observer who happens to be located within with the collimation cones of the jets. The jets emanating from a single massive star are so bright that they can be seen across the Universe out to the epoch when the first stars formed. Upcoming observations by the *Swift* satellite will have the sensitivity to reveal whether Pop III stars served as progenitors of gamma-ray bursts (for more information see <http://swift.gsfc.nasa.gov/>).

more recent counterparts. Consequently, the characteristic luminosity of galaxies or quasars is expected to decline with increasing redshift. GRB afterglows, which already produce a peak flux comparable to that of quasars or starburst galaxies at $z \sim 1-2$, are therefore expected to outshine any competing source at the highest redshifts, when the first dwarf galaxies formed in the Universe.

GRBs, the electromagnetically-brightest explosions in the Universe, should be detectable out to redshifts $z > 10$. High-redshift GRBs can be identified through infrared photometry, based on the Ly α break induced by absorption of their spectrum at wavelengths below $1.216 \mu\text{m} [(1+z)/10]$. Follow-up spectroscopy of high-redshift candidates can then be performed on a large aperture infrared telescope, such as *JWST*. GRB afterglows offer the opportunity to detect stars as well as to probe the metal enrichment level [45] of the intervening IGM. Recently, the ongoing *Swift* mission [46] has detected GRB050904 originating at $z \simeq 6.3$ [50], thus demonstrating the viability of GRBs as probes of the early Universe.

Another advantage of GRBs is that the GRB afterglow flux at a given observed time lag after the γ -ray trigger is not expected to fade significantly with increasing redshift, since higher redshifts translate to earlier times in the source frame, during which the afterglow is intrinsically brighter [26]. For standard afterglow lightcurves and spectra, the increase in the

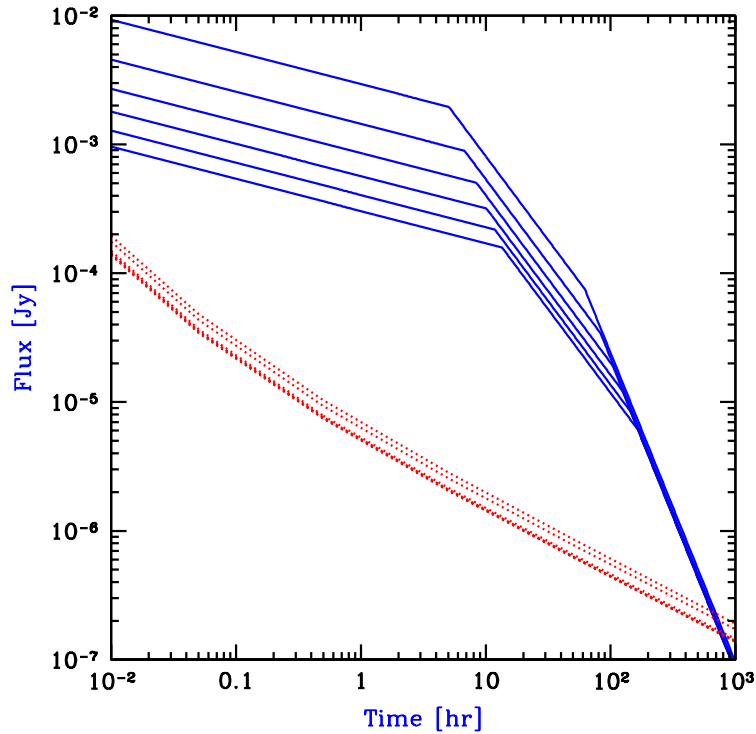


Fig. 16. GRB afterglow flux as a function of time since the γ -ray trigger in the observer frame (from Barkana & Loeb 2004a [5]). The flux (solid curves) is calculated at the redshifted Ly α wavelength. The dotted curves show the planned detection threshold for the *James Webb Space Telescope (JWST)*, assuming a spectral resolution $R = 5000$ with the near infrared spectrometer, a signal to noise ratio of 5 per spectral resolution element, and an exposure time equal to 20% of the time since the GRB explosion. Each set of curves shows a sequence of redshifts, namely $z = 5, 7, 9, 11, 13,$ and 15 , respectively, from top to bottom.

luminosity distance with redshift is compensated by this *cosmological time-stretching* effect [26, 5] as shown in Figure 16.

GRB afterglows have smooth (broken power-law) continuum spectra unlike quasars which show strong spectral features (such as broad emission lines or the so-called “blue bump”) that complicate the extraction of IGM absorption features. In particular, the continuum extrapolation into the Ly α damping wing during the epoch of reionization is much more straightforward for the smooth UV spectra of GRB afterglows than for quasars with an underlying broad Ly α emission line [5]. However, the interpretation regarding the neutral fraction of the IGM may be complicated by the presence of damped Ly α absorption by dense neutral hydrogen in the immediate environment of the GRB within its host galaxy [5, 97] and by the patchiness of the neutral IGM during reionization [79]. Since long-duration GRBs originate from the dense environment of active star formation, the associated damped Ly α absorption from their host galaxy was so-far always observed [84, 85], including in the most distant GRB at $z = 6.3$ [97].

Acknowledgement. I thank my collaborators on the work described in this review, Dan Babich, Rennan Barkana, Volker Bromm, Benedetta Ciardi, Mark Dijkstra, Richard Ellis, Steve Furlanetto, Zoltan Haiman, Jonathan Pritchard, George Rybicki, Dan Stark, Stuart Wyithe and Matias Zaldarriaga. I also thank Matt McQuinn for a careful reading of the manuscript.

References

1. Abel T, Bryan, G L, Norman M L (2002) *Science* **295**, 93
2. Allison A C, Dalgarno A (1969) *ApJ* **158**, 423
3. Angulo R, Baugh C M, Frenk C S, Lacey C G (2007) *ArXiv Astrophysics e-prints*, arXiv:astro-ph/0702543
4. Arons J, Wingert D W (1972) *ApJ* **177**, 1
5. Barkana R, Loeb A (2004a) *ApJ* **601**, 64
6. Barkana R, Loeb A (2004b) *ApJ* **609**, 474
7. Barkana R, Loeb A (2005a) *ApJL* **624**, L65
8. Barkana R, Loeb A (2005b) *ApJ* **626**, 1
9. Barkana R, Loeb A (2005c) *MNRAS* **363**, L36
10. Bennett C L et al. (1996) *ApJL* **464**, L1
11. Bertschinger E (2006) *Phys Rev* **D74**, 063509
12. Bharadwaj S and Ali S S (2004) *MNRAS* **352**, 142
13. Blake C, Glazebrook K (2003) *ApJ* **594**, 665
14. Bouwens R J, Illingworth G D, Blakeslee J P, Franx M (2006) *ApJ* **653**, 53
15. Bouwens R J, Illingworth G D (2006) *Nature* **443**, 189
16. Bouwens R J, Illingworth G D, Franx M, Ford H (2007) *ArXiv e-prints*, 707, arXiv:0707.2080
17. Bowman J D, Morales M F and Hewitt J N (2006) *ApJ* **638**, 20
18. Bromm V, Kudritzki R P, Loeb A (2001) *ApJ* **552**, 464
19. Bromm V, Larson R B (2004) *Ann Rev Astron & Astrophys* **42**, 79
20. Bromm V, Loeb A (2003) *Nature* **425**, 812
21. Bromm V, Loeb A (2003) *ApJ* **596**, 34
22. Bromm V, Loeb A (2004) *New Astronomy* **9**, 353
23. Ciardi B, Ferrara A, White S D M (2003) *MNRAS* **344** L7
24. Cole S, et al (2005) **362**, 505
25. Cuby J-G, Hibon P, Lidman C, Le Fèvre O, Gilmozzi R, Moorwood A, van der Werf P (2007) *A & A* **461**, 911
26. Ciardi B, Ferrara A, White S D M (2003) *MNRAS* **344**, L7
27. Di Matteo T, Perna R, Abel T and Rees M J (2002) *ApJ* **564**, 576
28. Dijkstra M, Haiman Z, Spaans M (2006) *ApJ* **649**, 14
29. Dijkstra M, Lidz A, Wyithe J S B (2007) *MNRAS* **377**, 1175
30. Diemand J, Moore B, & Stadel J (2005) *Nature* **433**, 389 (2 005)
31. Dow-Hygelund C C, et al (2007) *ApJ* **660**, 47
32. Eisenstein D, et al (2005) *ApJ* **633**, 560
33. Ellis R S (2007) *ArXiv Astrophysics e-prints*, arXiv:astro-ph/0701024
34. Fan X, et al (2002) *AJ*, **123**, 1247
35. Fan X, et al (2003) *AJ* **125**, 1649
36. Fan X, et al. (2005) *AJ* **132**, 117
37. Fan X, Carilli C L, Keating B (2006) *Ann Rev Astron & Astrophys* **44**, 415
38. Field G B (1958) *Proc. IRE* **46**, 240

39. Field G B (1959), *ApJ* **129**, 551
40. Frebel A, Johnson J L, Bromm V (2007) *MNRAS* **380**, L40
41. Furlanetto S R, Loeb A (2004) *ApJ* **611**, 642
42. Furlanetto S R, Oh S P, Briggs F H (2006), *Phys Rep* **433**, 181
43. Furlanetto S R, Zaldarriaga M and Hernquist L (2004) *ApJ* **613** 1
44. Fukugita M, Kawasaki M (1994), *MNRAS* **269**, 563
45. Furlanetto S R, Loeb A (2003) *ApJ* **588**, 18
46. Gehrels N, et al (2004) *ApJ* **611**, 1005
47. Glazebrook K, Blake C (2005) *ApJ* **631**, 1
48. Haiman Z, Loeb A (1997) *ApJ* **483**, 21
49. Haiman Z, Spaans M (1999) *ApJ* **518**, 138
50. Haislip J, et al (2006) *Nature* **440**, 181
51. Heger A, Fryer C L, Woosley S E, Langer N, & Hartmann D H (2003) *ApJ* **591**, 288
52. Hirata C M (2006) *MNRAS* **367**, 259
53. Hogan C J, Rees M J (1979) *MNRAS* **188**, 791
54. Horton A, Parry I, Bland-Hawthorn J, Cianci S, King D, McMahon R, Medlen S (2004) *Proc of the SPIE* **5492**, 1022
55. Hu W, Haiman Z (2003) *Phys Rev* **D68**, 063004
56. Iliiev I T, Shapiro, P R, Mellema G, Pen U-L, McDonald P, & Bond J R (2007) *ArXiv e-prints*, 708, arXiv:0708.3846
57. Iye M, et al (2006) *Nature* **443**, 186
58. Kaiser N (1984) *ApJL* **284**, 9
59. Kaiser N (1987) *MNRAS* **227**, 1
60. Kamionkowski M, Spergel D N, Sugiyama N (1994), *ApJL* **426**, 57
61. Kashikawa N, et al (2006) *ApJ* **648**, 7
62. Lamb D Q, Reichart D E (2000) *ApJ* **536**, 1
63. Lewis A, Challinor A (2007), *ArXiv Astrophysics e-prints*, arXiv:astro-ph/0702600
64. Lidz A, Oh S P, Furlanetto S R (2006), *ApJL* **639**, 47
65. Loeb A (2006), "First Light", extensive review for the SAAS-Fee 2006 Winter School, *ArXiv Astrophysics e-prints*, arXiv:astro-ph/0603360
66. Loeb A, Rasio F A (1994) *ApJ* **432**, 52
67. Loeb A, Rybicki G B (1999) *ApJ* **524**, 527
68. Loeb A, Zaldarriaga M (2004), *Phys Rev Lett* **92**, 211301
69. Loeb A, Zaldarriaga M (2005) *Phys Rev* **D71**, 103520
70. Madau P, Meiksin A and Rees M J (1997) *ApJ* **475**, 429
71. Malhotra S, Rhoads J E (2002) *ApJL* **565**, L71
72. Malhotra S, Rhoads J E (2004) *ApJL* **617**, L5
73. Mellema G, Iliiev I T, Pen U-L, Shapiro P R (2006) *MNRAS* **372**, 679
74. Mesinger A, Haiman Z (2004) *ApJL* **611**, 69
75. Mesinger A, Furlanetto S (2007) *ArXiv e-prints*, 708, arXiv:0708.0006
76. McQuinn M, Zahn O, Zaldarriaga M, Hernquist L, Furlanetto S R (2006) *ApJ* **653**, 815
77. McQuinn M, Lidz A, Zahn O, Dutta S, Hernquist L, Zaldarriaga M (2007a) *MNRAS* **377**, 1043
78. McQuinn M, Hernquist L, Zaldarriaga M, Dutta S (2007b) *MNRAS* **381**, 75
79. McQuinn M, Lidz A, Zaldarriaga M, Hernquist L, Dutta S (2007c) *ArXiv e-prints*, 710, arXiv:0710.1018
80. Naoz S and Barkana R (2005) *MNRAS* **362**, 1047
81. Oh S P (2001) *ApJ* **553**, 499
82. Pritchard J R, Furlanetto S R (2006) *MNRAS* **367**, 1057

83. Pritchard J R, Furlanetto S R (2007), MNRAS **376**, 1680
84. Prochaska J X, et al (2007) ApJS **168**, 231
85. Prochaska, J X, Chen H-W, Dessauges-Zavadsky M, Bloom J S (2007) ApJ **666**, 267
86. Purcell E M and Field G B (1956) ApJ **124**, 542
87. Rybicki G B, Loeb A (1999) ApJL **520**, L79
88. Schneider R, Omukai K, Inoue A K, Ferrara A (2006) MNRAS **369**, 1437
89. Scott D, Rees M J (1990) MNRAS **247**, 510
90. Seo H-J, Eisenstein D J (2003) ApJ **598**, 720
91. Seo H-J, Eisenstein, D J (2005) ApJ **633**, 575; **665**, 14
92. Shapiro P R, Giroux M L (1987) ApJL, **321**, 107
93. Shapiro P R, Giroux M L, Babul A (1994) ApJ **427**, 25
94. Stark D P, Ellis R S, Richard J, Kneib J-P, Smith G P, Santos M R (2007) ApJ **663**, 10
95. Stark, D P, Loeb A, Ellis R S (2007) ApJ **668**, 627
96. Taniguchi Y, et al (2005) PASJ **57**, 165
97. Totani T, Kawai N, Kosugi G, Aoki K, Yamada T, Iye M, Ohta K, Hattori T (2006) PASJ **58**, 485
98. Trac H, Cen R (2006), ArXiv Astrophysics e-prints, arXiv:astro-ph/0612406
99. Tumlinson J, Shull J M (2000), ApJL **528**, 65
100. Spergel D N, et al (2006) ApJS **170**, 377
101. Wouthuysen S A (1952) AJ **57**, 31
102. White R L, Becker R H, Fan X, Strauss M A (2003) AJ **126**, 1
103. Willis J P, Courbin F, Kneib J-P, Minniti D (2006) New Astronomy Review **50**, 70
104. Willis J P, Courbin F, Kneib J P, Minniti D (2007) ArXiv e-prints, 709, arXiv:0709.1761
105. Wyithe J S B, Loeb A (2004a) Nature **427**, 815
106. Wyithe J S B, Loeb A (2004b) Nature **432**, 194
107. Wyithe J S B, Loeb A, Barnes D G (2005) ApJ **634**, 715
108. Wyithe J S B, Loeb A (2007a) MNRAS **375**, 1034
109. Wyithe J S B, Loeb A (2007b) ArXiv e-prints, 708, arXiv:0708.3392
110. Wyithe J S B, Loeb A, Schmidt B (2007) ArXiv e-prints, 705, arXiv:0705.1825
111. Wyithe J S B, Loeb A, Geil P (2007) ArXiv e-prints, 709, arXiv:0709.2955
112. Tegmark M et al (1997) ApJ **474**, 1
113. Zahn O, Lidz A, McQuinn M, Dutta S, Hernquist L, Zaldarriaga M and Furlanetto S R (2006) ApJ **654**, 12
114. Zhang W, Woosley S, MacFadyen A I (2003) ApJ **586**, 356
115. Zygelman B (2005) ApJ **622**, 1356